Article

A Nickel-Containing Polyoxomolybdate as an Efficient Antibacterial Agent for Water Treatment

Jiangnan Chang †, Mingxue Li †, Jiyuan Du, Min Ma, Cuili Xing, Lin Sun * and Pengtao Ma *

Henan Key Laboratory of Polyoxometalate Chemistry, College of Chemistry and Chemical Engineering, Henan University, Kaifeng 475004, China
* Correspondence: sunlin@vip.henu.edu.cn (L.S.); mpt@henu.edu.cn (P.M.)
† These authors contributed equally to this work.

Abstract: In view of the water pollution issues caused by pathogenic microorganisms and harmful organic contaminants, nontoxic, environmentally friendly, and efficient antimicrobial agents are urgently required. Herein, a nickel-based Keggin polyoxomolybdate $[Ni(L)(HL)]_2H[PMo_{12}O_{40}]\,4H_2O$ (**1**, HL = 2-acetylpyrazine thiosemicarbazone) was prepared via a facile hydrothermal method and successfully characterized. Compound **1** exhibited high stability in a wide range of pH values from 4 to 10. **1** demonstrated significant antibacterial activity, with minimum inhibitory concentration (MIC) values in the range of 0.0019–0.2400 µg/mL against four types of bacteria, including *Staphylococcus aureus* (*S. aureus*), *Bacillus subtilis* (*B. subtilis*), *Escherichia coli* (*E. coli*), and *Agrobacterium tumefaciens* (*A. tumefaciens*). Further time-kill studies indicated that **1** killed almost all (99.9%) of *E. coli* and *S. aureus.* Meanwhile, the possible antibacterial mechanism was explored, and the results indicate that the antibacterial properties of **1** originate from the synergistic effect between $[Ni(L)(HL)]^+$ and $[PMo_{12}O_{40}]^{3-}$. In addition, **1** presented effective adsorption of basic fuchsin (BF) dyes. The kinetic data fitted a pseudo-second-order kinetic model well, and the maximum adsorption efficiency for the BF dyes (29.81 mg/g) was determined by the data fit of the Freundlich isotherm model. The results show that BF adsorption was dominated by both chemical adsorption and multilayer adsorption. This work provides evidence that **1** has potential to effectively remove dyes and pathogenic bacteria from wastewater.

Keywords: polyoxomolybdate; antibacterial activity; antibacterial mechanism; adsorption properties

1. Introduction

In recent years, industrialization and urbanization have deteriorated water quality, resulting in a higher number of pollutants in the water, such as pathogenic bacteria, organic pollutants, and heavy metal ions [1–3]. Pathogenic bacteria are one of the most common contaminants in wastewater. Meanwhile, the widespread use of antibiotics not only leads to an increase in bacterial resistance but may also result in the emergence of super bacteria, thereby posing a threat to global public safety and the ecological environment [4,5]. For the last few years, a tremendous amount of effort has been devoted to the design of antimicrobial materials [6–9]. At the same time, significant amounts of co-products such as various organic dyes have been released into water due to the rapid development of the dyeing and printing industry, causing serious industrial wastewater contamination globally. Therefore, there is an urgent demand for the removal of harmful dyes from polluted water to alleviate environmental issues. To date, many techniques and methods have been utilized for the removal of toxic dyes, including adsorption, photocatalysis, and biodegradation [10]. Remarkably, the adsorption method has been extensively applied for the treatment of dye wastewater because of its low cost, simple operation, and practicality [11–13]. It is essential to remove contaminants from water before releasing it into the environment. Thus, it is urgent to construct multifunctional materials with both antibacterial performance and dye adsorption properties [14].

Polyoxometalates (POMs) are unique nanoscale polyanionic clusters comprising early transition metal oxides that have potential application in biological and medical areas, material science, and water treatment [15,16]. Given their adjustable structure and extensive physiochemical properties, considerable efforts and studies have been devoted to the construction of POM-based hybrids and nanocomposites with antimicrobial and adsorptive properties. In 2018, Rompel's group reported the antibacterial activity of 29 different POMs against *Moraxella catarrhalis*, and the Preyssler-type polyoxotungstate $[NaP_5W_{30}O_{110}]^{14-}$ demonstrated excellent antibacterial activity with an MIC of 1 µg/mL [17]. In 2020, our group reported two Keggin-type Co-POMs with significant antibacterial properties, namely $[Co(L)_2]_3[PMo_{12}O_{40}]$ and $[Co(L)_2]_3[PW_{12}O_{40}]$ [18]. In 2021, an aluminum-substituted Keggin $[Al(H_2O)GeW_{11}]^{4-}$ was synthesized by Rompel's group, and the Al-POM indicated enhanced antibacterial activity compared with simple aluminum salt against *Moraxella catarrhalis* (MIC = 4 µg/mL) and Gram-positive *Enterococcus faecalis* (MIC = 128 µg/mL), respectively [19]. Obviously, both polyoxomolybdates and polyoxotungstates exhibit excellent antibacterial activity. In addition, POM-based composites also exhibit adsorption properties for dye removal. Dong's group presented a feasible and versatile approach to introduce POMs to construct a functionalized membrane via a novel sol-gel method, and this material effectively removed reactive black 5 dyes [20]. In 2020, Mardiyanto's group investigated an Ni-Fe layered double hydroxide (LDH) intercalated by Keggin-type POM $[SiW_{12}O_{40}]^{4-}$, and the material showed a large adsorption capacity for malachite green (MG) [21]. However, little information is available on POMs with both antimicrobial and adsorption properties. Hence, the design and construction of POMs-based materials are vital to realizing bifunctionalization of such materials.

POM-based inorganic-organic hybrids exhibit enhanced antimicrobial and adsorption properties compared to pure POMs [22,23]. Among the organic ligands, 2-acetylpyrazine thiosemicarbazone (HL) showed excellent antibacterial activity in pharmacological applications, being a superior candidate for the construction of POM-based inorganic-organic hybrids [24–27]. This study aimed to construct a multifunctional POM compound with both antibacterial performance and dye adsorption properties. An Ni-based polyoxomolybdate compound $[Ni(L)(HL)]_2H[PMo_{12}O_{40}]$ $4H_2O$ (**1**) was constructed using the facile hydrothermal method and systematically characterized. **1** not only showed excellent antibacterial activity but also exhibited adsorption properties for BF dyes, which supports the use of POMs as water purification materials in the killing of microorganisms and removal of organic contaminants synchronously. The antibacterial activities and adsorption performance of **1** were explored in detail. Furthermore, the possible antibacterial and adsorption mechanisms of **1** were also proposed on the basis of the experimental results.

2. Results and Discussion

X-ray single-crystal diffraction analysis shows that **1** crystallizes in the space group P-1 [28,29], as shown in Table S1. The molecular structure of **1** contains two $[Ni(L)(HL)]^+$ cations, one H^+, one Keggin $[PMo_{12}O_{40}]^{3-}$ anion, and four lattice water molecules (Figure 1A). The coordination configuration of the Ni(II) ions was calculated using the SHAPE 2.1 program [28], as shown in Table S2, and the result indicates that the Ni(II) centers are located in a distorted octahedron geometry. In **1**, each six-coordinate Ni(II) ion is surrounded by four N atoms and two S atoms from two 2-acetylpyrazine thiosemicarbazone ligands (Ni–N: 2.026–2.102 Å, Ni–S: 2.391–2.398 Å, ∠S–Ni–S: 93.88 (2)°, ∠N–Ni–S: 83.2 (1)–160.9 (1)°, ∠N–Ni–S: 77.9 (1)–172.3 (1)°). Meanwhile, the two dihedral angles of (Ni1–S1–C1–N2–N3)···(Ni1–N3–C2–C4–N5) and (Ni1–N10–C11–C9–N8)···(Ni1–S2–C8–N7–N8) were found to be about 2.436° and 0.659°, respectively. Obviously, each HL ligand includes one imine and one pyrazine group, which contribute to the formation of hydrogen bonds, and five kinds of H-bond interactions (N7–H7···O1, N6–H6A···O1, N6–H6B···O5, N1–H1A···O1W, N1–H1A···O10) were observed in the structure of **1**. The $[Ni(L)(HL)]^+$ cations and $[PMo_{12}O_{40}]^{3-}$ polyoxoanions are connected by hydrogen bonding (Figure 1B), with further stacking to form the layered structure (Figure S1A,B).
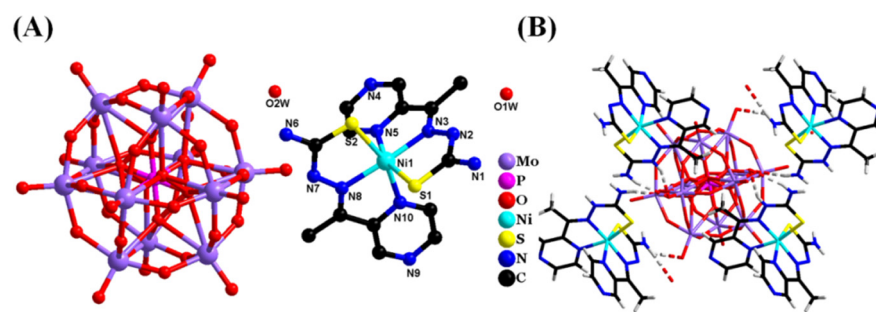
Figure 1. (**A**) The molecular structure of **1**. (**B**) H-bond interactions between $[Ni(L_2)(HL_2)]^+$ and $[PMo_{12}O_{40}]^{3-}$.

FT-IR spectroscopy was employed to identify the functional groups of **1** (Figure 2A). The peaks at 3174 cm^{-1} and in the region of 1608–1395 cm^{-1} belong to the stretching vibration of ν(N–H) and ν(C=N) of HL, and the (P–Oa) vibrations of **1** can be observed at 1158–1057 cm^{-1} [30]. Additionally, three characteristic vibration bands of **1** at 953, 840, and 786 cm^{-1} are assigned to the asymmetric stretching vibrations of ν(Mo–O$_d$), ν(Mo–O$_b$–Mo), and ν(Mo–O$_c$–Mo) [31], respectively. The characteristic absorption bands prove the existence of the $[PMo_{12}O_{40}]^{3-}$ anion in the structure of **1**. In addition, the Raman spectrum (Figure 2B) of **1** shows main characteristic vibration bands at 814, 883, and 935 cm^{-1}, which correspond to the symmetrical stretching Mo–O–Mo, Mo=O, and P–O [32,33], respectively. Hence, it can be concluded that the Keggin-type POM compound was successfully prepared.
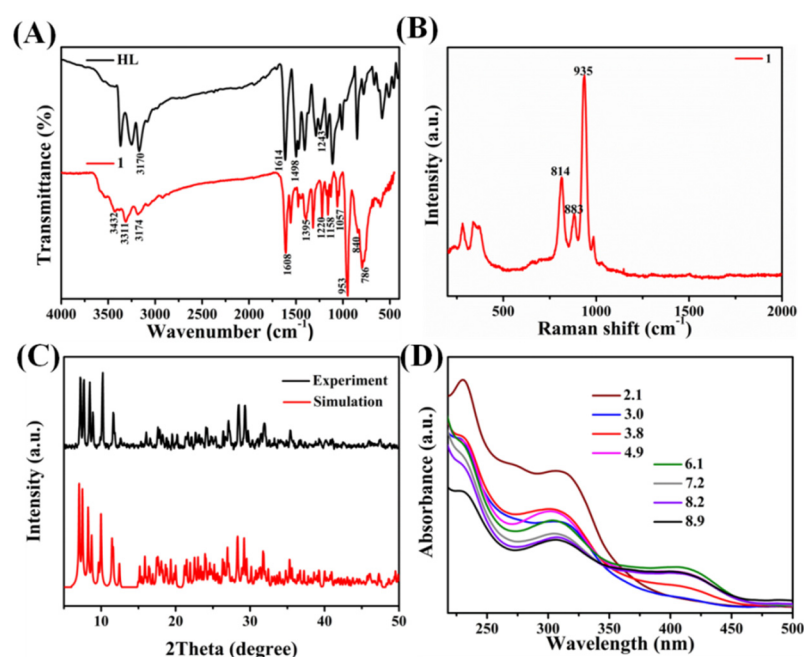
Figure 2. (**A**) Infrared spectra of **1**. (**B**) Raman spectroscopy of **1**. (**C**) PXRD pattern of **1** and (**D**) UV−Vis spectra of **1** (numbers represent the pH value).

The X-ray diffraction (XRD) spectra were used to confirm the phase purity of **1**. The XRD patterns for **1** from the experiments are in accordance with the simulation results (Figure 2C).

To evaluate the stability of **1**, the ultraviolet–visible (UV-vis) spectroscopy at different pH values from 2 to 12 was investigated in detail. The spectra of **1** indicate three characteristic bands in the region of 200–500 nm. The bands at 230 and 307 nm are attributed to the charge transfer transition of Od→Mo and Ob, Oc→Mo bands [34], respectively. Meanwhile,

weak absorption is seen at 411 nm, which may be due to the ligand to metal charge transfer (LMCT) transitions [35]. When pH value is 3.8, the band strength at 411 nm becomes weak. The peak gradually flattens as the pH value decreases (Figure 2D). In addition, a weak band at 230 nm is observed at pH 9.9 (Figure S2B), and the peak disappears as the pH value increases, indicating that the POM framework was decomposing. Based on these experimental results, **1** possesses good stability (pH = 4–10).

The results of the X-ray photoelectron spectroscopy (XPS) analysis demonstrate the detailed chemical compositions of the synthetic compound and the valence state of these elements. Figure 3A shows that the elements of Ni, O, N, C, P, Mo, and S exist in **1**. The XPS spectrum of Ni 2p suggests two obvious peaks at the binding energies of 871.7 and 854.2 eV (Figure 3B), which are assigned to Ni^{2+} 2p1/2 and Ni^{2+} 2p3/2, respectively [36]. Additionally, the presence of two satellite peaks in the Ni 2p XPS spectra further demonstrates the existence of octahedrally coordinated Ni (II) ions [37,38].
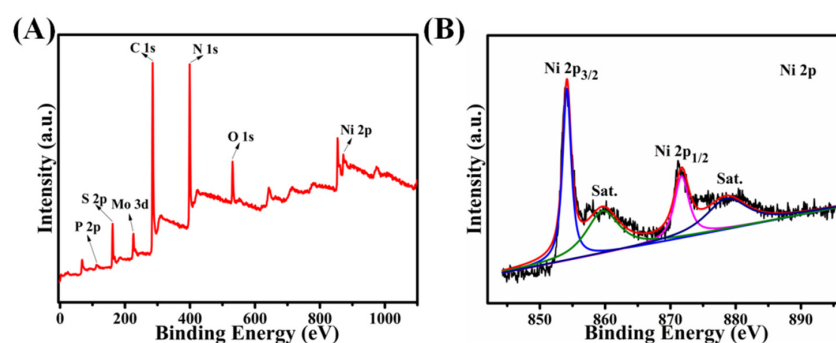

Figure 3. (**A**) XPS spectra of **1**. (**B**) Detailed spectrum of the nickel Ni 2p peaks of **1** (red: Ni 2p; blue: Ni 2p3/2; pink: Ni 2p1/2; black: standard curve).

Scanning electron microscopy (SEM) images were used to investigate the morphology of **1**. **1** has a quadrilateral structure with a flat surface and most crystal compounds show a similar shape (Figure 4A,B). Furthermore, **1** showed a range of widths between 50 and 86 μm and lengths between 95 and 190 μm, respectively. Additionally, the SEM elemental mappings of Ni (green), Mo (red), and P (yellow) are observed in the same micrometer region and these components are uniformly scattered in **1**. The elemental mappings show the color intensity of the components, confirming that the content of the Mo element is higher than that of the Ni and P elements (Figure 4C–E), which is in agreement with the ICP analysis.
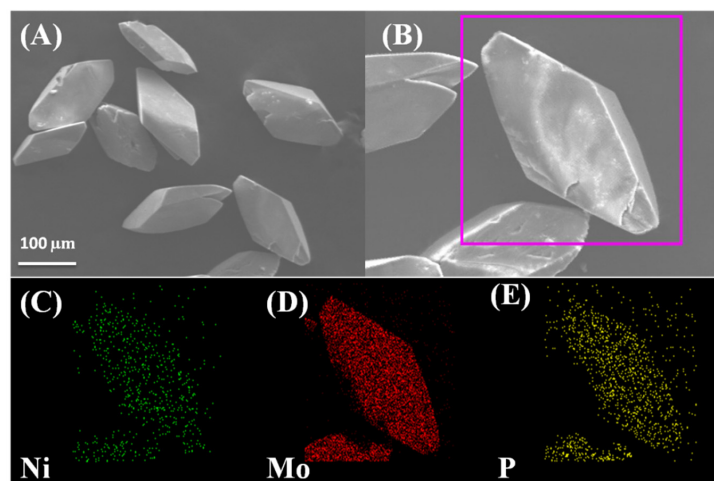

Figure 4. (**A**,**B**) The SEM image of **1** (the pink box represents the selected region). (**C**–**E**) The SEM elemental mappings of Ni, Mo, and P in **1**.

2.1. Antibacterial Properties

In this study, the antibacterial activities were assessed using four bacterial strains (*E. coli*, *A. tumefaciens*, *S. aureus*, and *B. subtilis*) and the disc diffusion method to confirm the MIC values. The inhibition zone diameters of **1** against *E. coli* bacteria and *B. subtilis* bacteria were measured (Figure S3C). **1** showed high antibacterial activities against both *E. coli* bacteria and *B. subtilus* bacteria, with two similar inhibition zone diameters of 20 mm at a concentration of 4 mg/mL. As the concentrations decreased, the inhibition zone diameters diminished little by little. To explore the antibacterial efficiency of the different components, the MIC values were explored, including HL, $Ni(ClO_4)_2 \cdot 6H_2O$, $H_3[PMo_{12}O_{40}]$ (Pmo_{12}), **1**, two reference medicines, amoxicillin trihydrate (Am), and kanamycin sulfate (Kan), as illustrated in Table 1. It can be seen that a single component nickel ion exhibited inferior antibacterial activity, with a high MIC value. In comparison, ligand HL and $H_3[PMo_{12}O_{40}]$ demonstrated lower MIC values, indicating that they have higher antibacterial activity than nickel salts. It is worth noting that the MIC values of **1** were 0.015 and 0.24 μg/mL against the Gram-negative bacteria *E. coli* and *A. tumefacies* and 0.0019 and 0.03 μg/mL against the Gram-positive bacteria *S. aureus* and *B. subtilis*, respectively, which demonstrates **1** exhibited high-efficiency antibacterial activities. At the same time, compared with Am and Kan, **1** possessed a lower MIC value, indicating that **1** may be used as a potential antibacterial agent.

Table 1. In vitro antibacterial activity of **1**.

Microorganism	MIC (μg/mL)					
	HL	$Ni(ClO_4)_2 \cdot 6H_2O$	$H_3[PMo_{12}O_{40}]$	1	Am	Kan
E. coli	0.23	31.25	0.48	0.015	0.90	7.80
A. tumefaciens	0.45	125.00	0.90	0.24	3.90	1.90
B. subtilis	0.12	15.60	0.90	0.030	0.24	0.24
S. aureus	0.12	7.80	0.12	0.0019	0.24	0.48

2.2. Time-Kill Studies

In order to further evaluate the bactericidal or bacteriostatic ability of **1**, time-kill studies were carried out using the viable cell count method (VCC). The numbers of *E. coli* bacterium and *S. aureus* bacterium declined as time increased (Figure 5A,B). After being exposed to **1** for 4 h, about 81% of the *E. coli* bacterium were killed while the killing rate of *S. aureus* bacterium reached 97%, indicating that **1** could kill *S. aureus* bacterium quickly. As expected, both types of bacteria were nearly killed within 6 h after treatment with **1**. In addition, it is concluded that **1** differs in its sensitivity to *S. aureus* and *E. coli* bacteria. Meanwhile, the experimental results were also analyzed by statistical analysis (Figure S3A,B), indicating that **1** showed significant antibacterial activity against *S. aureus* and *E. coli* bacteria.
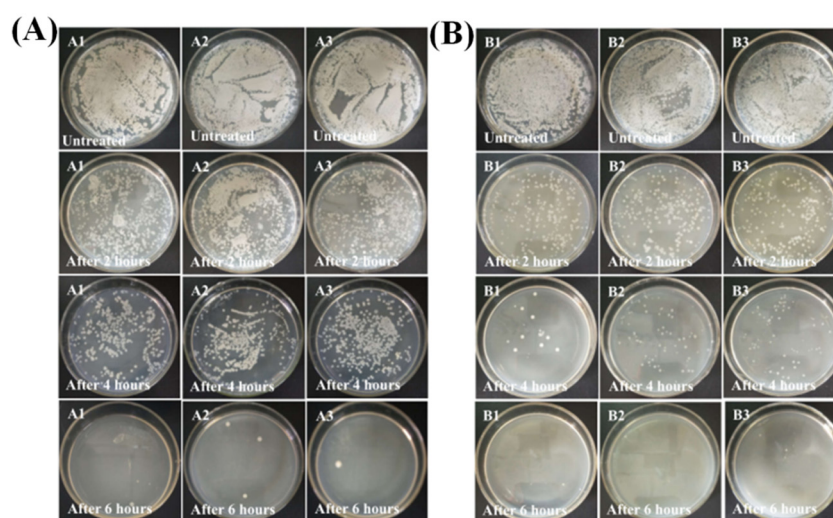
Figure 5. (**A**) Photographs of *E. coli* after different treatment times (0, 2, 4 and 6 h). (**B**) Photographs of *S. aureus* after different treatment times (0, 2, 4 and 6 h). A1–A3 and B1–B3 represent three parallel experiments.

2.3. Adsorption Performances

To evaluate whether the adsorption capacity of **1** was affected by different factors, adsorption experiments were performed. The size range of the solid crystals was 50–200 μm in the experiments. Some influencing factors (dye concentrations, adsorption dosage, different dyes and pH values) were considered in the experiments. To explore the optimal mass concentrations of the BF dyes, **1** (20 mg) was added to 50 mL of aqueous solutions of BF at room temperature with different mass concentrations of 5, 10, and 15 mg L^{-1}. It can be seen that the content of the BF dyes showed an obvious decrement (71%) of 15 mg L^{-1} in the absorption spectra (Figure S4A), which signifies that **1** exhibited a better adsorption performance. However, **1** removed about 61% and 42% of the BF dyes at the BF concentrations of 5 and 10 mg/L, respectively. Additionally, it should be mentioned that the dye concentration decreased rapidly during the first 30 min, which may be attributed to a large number of active sites of the dye being occupied via electrostatic interaction [10], then gradually reduced after 30 min. By analyzing the C/C_0 versus BF concentration and contact time, the C/C_0 value decreased with the increase in the contact time until the maximum adsorption was observed at 90 min for all concentrations of the BF dyes. Finally, the adsorption reached equilibrium and there was almost no further increase in the adsorption. Commonly, the ratio between the initial number of BF molecules and the available surface area is large at higher concentrations. Thereby, fractional adsorption relies on the initial concentration of BF dyes. However, fewer sites of adsorption are available at lower concentrations, thus dye removal depends on the concentration of dyes [39]. According to these results, it appears that the adsorption uptake is sharp for the first 30 min, after which it goes through a slower adsorption process, thereby obtaining saturation at 90 min [27,39]. The whole adsorption step is divided into two processes, including the first fast-speed surface adsorption and the slower diffusion adsorption inside the particles during the second period.

The adsorption dosage also plays an important role in the removal of organic dyes. **1** showed a distinct adsorption capacity of 0.2, 0.4, and 0.8 mg/mL with a removal ratio of 69.6%, 79.9%, and 67.2% in the dark for 90 min (Figure 6A). Moreover, according to further simulation and analysis of the data, the maximum adsorption capacity of the above adsorption dosages was 26.41, 29.81, and 25.85 mg/g, respectively. The adsorption ability of **1** decreased with an increase in the adsorbent concentration from 0.4 to 0.8 mg/mL. This may have been caused by a reduction in the specific surface area of POM and available adsorption sites for BF dyes due to the enhanced repulsive interaction and agglomeration

between POM particles [40,41]. In addition, to further verify this conclusion, the adsorbent concentration (1 mg/mL) was utilized to further explore the adsorption capacity of **1**, and the adsorption rate was 62.07% according to the removal efficiency formula (Equation (S2)). The results demonstrated that the optimal concentration of **1** was 0.4 mg/mL for BF adsorption.
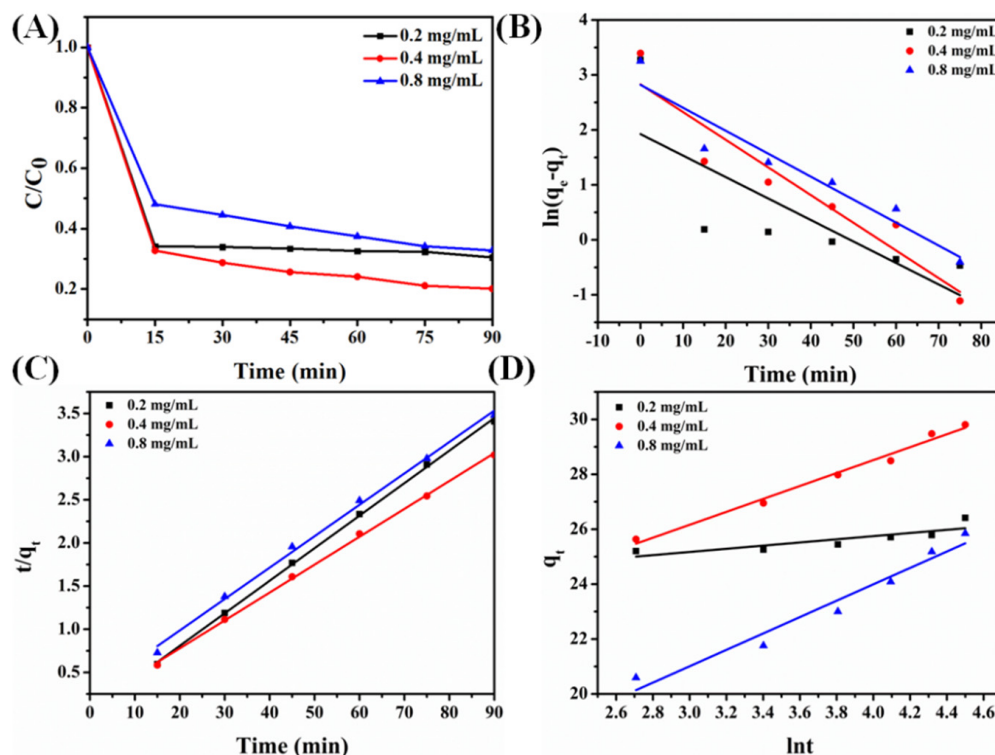

Figure 6. (**A**) Adsorption performance of **1** for BF solution. (**B**–**D**) Kinetic plots of BF adsorption by the pseudo−first−order kinetics model, pseudo−second−order kinetics model, and the Elovich equation.

Additionally, the adsorption ability of **1** for the other organic dyes was also investigated under dark conditions at room temperature. **1** showed a selective adsorption capacity for the methylene blue (MB), gentian violet (GV), and BF dyes, with removal ratios of 46.6%, 69%, and 90.1% (Figure S4B), respectively. However, the removal ratio of methyl orange (MO) was close to 0, which is consistent with the result of MO dye removal in a previous report [42,43]. As a result, **1** can efficiently and selectively remove cationic dyes from wastewater.

The adsorption performances of **1** for the BF dyes were tested under acidic, alkaline, and neutral solution environments since the pH values of natural wastewater varied. As shown in Figure S4C, **1** showed the best adsorption performance in the neutral solution and removed about 41.8% of the BF dyes through adsorption. However, **1** showed almost no adsorption for BF dyes under the acidic and alkaline circumstances, which is also consistent with previous reports [10,44].

To confirm the stability of **1** before and after BF adsorption, a series of tests were executed. The SEM test results indicate that the morphology of **1** did not change after adsorption, and the test result of the element mapping reveal that the Ni, Mo, and P elements existed in **1** after adsorption. Furthermore, the peak positions from the IR and Raman spectrum were nearly constant before and after adsorption, which indicates that the functional groups of **1** did not change. The above test results confirm that the structure of **1** remained after adsorption. The SEM test of **1** after adsorption (Figure S5) and the IR

and Raman spectrum of **1** after adsorption (Figure S6) are shown in the Supplementary Materials.

For practical applications of adsorbents, it is vital to explore their stability and regeneration ability during the adsorption process. The adsorbent **1** could be regenerated by simple dry treatment at 60 °C for 180 min. **1** retained a high removal efficiency over three cycles. As depicted in Figure S7, the adsorption capacities decreased for each new cycle after dry treatment. The original adsorption capacity of **1** for the BF dyes was 29.81 mg/g, which then dropped to 24.45 mg/g after three cycles. Consequently, **1** showed fine stability and regeneration for BF adsorption.

The UV–vis spectra of the dye solution at 330-min intervals are presented in Figure S4D. After 330 min of adsorption, the absorption peaks of the wavelength at 542 nm decreased continuously and the dye solution became almost colorless, indicating that most of the BF dyes in water were removed. The cationic dye adsorption is possibly attributed to electrostatic interaction, $\pi \cdots \pi$ interactions, hydrophobic interaction, and hydrogen bond [20,41].

2.3.1. Adsorption Kinetics

By fitting the experimental data to the three models (Figure 6B–D), we report the kinetic parameters of BF adsorbed onto **1** (Table 2). It can be seen that the pseudo-second-order rate expression ($R^2 > 0.99$) is in good agreement with the experimental data for BF. The higher coefficients of the pseudo-second-order model show that the adsorption process of **1** for the BF dyes was mainly governed by chemisorption. Moreover, the adsorption rate was found to be slow due to the occupied active sites on the surface of **1** as the solution concentration increased.

Table 2. The kinetic parameters of BF adsorption on **1**.

Concentrations	Pseudo-First-Order		Pseudo-Second-Order		The Elovich Equation	
	K	R^2	K	R^2	K	R^2
0.2 mg/mL	−0.03905	0.51277	0.03769	0.99921	0.5777	0.66326
0.4 mg/mL	−0.05034	0.88066	0.03231	0.99896	2.3566	0.98221
0.8 mg/mL	−0.04577	0.90885	0.03665	0.99697	2.9195	0.95618

2.3.2. Equilibrium Results

The equilibrium curves (Figure 7) of **1** for the BF dyes were fitted with the Langmuir, Freundlich, Dubinin–Radushkevich, and Temkin models, and the fitting parameters are displayed in Table 3. It shows that the four used models presented different values of R^2. Moreover, the Freundlich model presented a higher value than the Dubinin–Radushkevich, Temkin, and Langmuir models; thus, it can be assumed that the BF molecules were not distributed equally. The maximum adsorption capacity of **1** for the BF dyes was 29.81 mg/g.

Table 3. The isotherm parameters for the adsorption of BF dyes.

	Langmuir Isotherm Model		Freundlich Isotherm Model		Dubbin–Radushkevich Isotherm Model		Temkin Model	
	K	R^2	K	R^2	K	R^2	K	R^2
BF	0.01451	0.6249	0.82337	0.95106	-2.67931×10^{-6}	0.85368	10.87912	0.92921

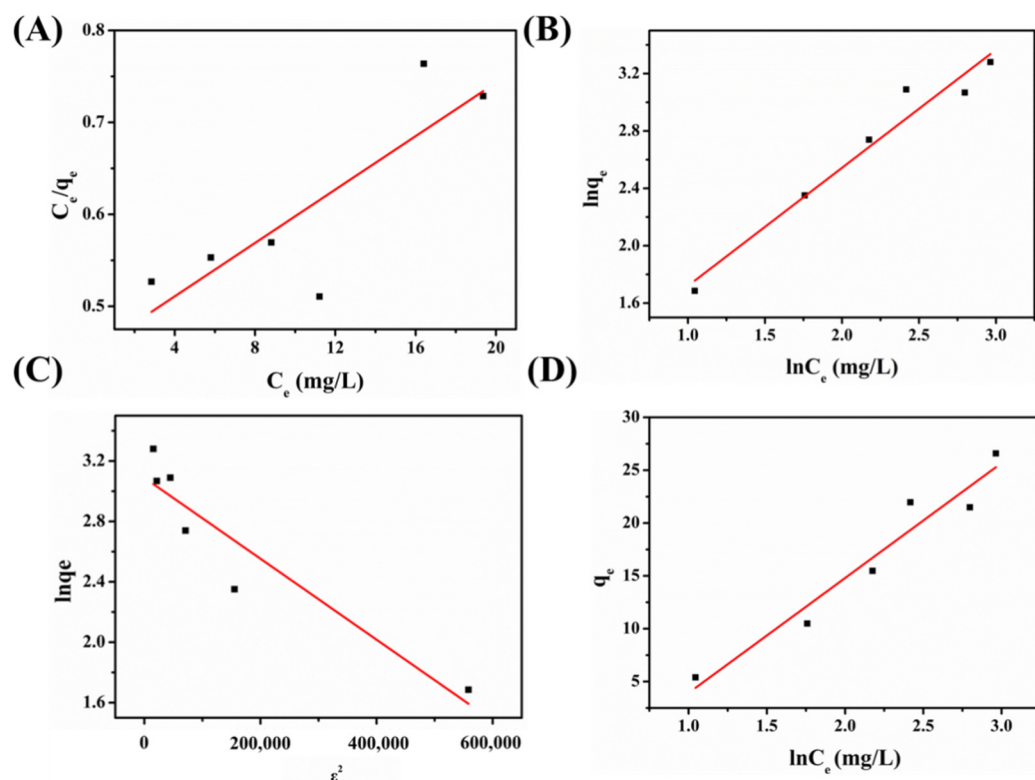**Figure 7.** (**A**–**D**) Isotherm plots of **1** for the BF adsorption by the Langmuir, Freundlich, Dubinin–Radushkevich, and Temkin models.

2.4. Probable Action Mechanisms

The Gram-negative bacteria *E. coli* possesses a dense lipopolysaccharide layer (outer membrane), containing lipid, oligosaccharide, and polysaccharide molecules whereas *S. aureus*, a type of Gram-positive bacterium, has a thicker peptidoglycan layer without any outer membrane [45]. Moreover, the outer membrane provides the cell with a strong permeability barrier, which can resist macromolecules and hydrophobic molecules [18]. Hence, to better understand the antibacterial mechanism of **1**, *E. coli* was selected as a model to study the effect of **1**. In general, the negatively charged bacterial cell wall provides antibacterial materials with coordination sites, facilitating the interaction between the membrane and compound. Thus, if the balance of the potential on the bacterial cell surface is disrupted, which in turn changes the permeability and integrity of the cells, the destruction of the cell wall/membrane can cause an outflow of intracellular components, leading to cell death [46,47].

To intuitively observe the interaction of cells with **1**, SEM images were used to observe the morphological changes in the *E. coli* cells. The untreated *E. coli* cells exhibited a natural rod-shaped surface and smooth appearance with complete cell walls/membranes (Figure 8A). Comparatively, obvious morphological and physical damage of cells was observed after treatment with **1** (Figure 8B), including severe perforation and disturbance of the cell membranes. The SEM image results indicate that **1** led to serious damage to the bacterial morphology, further damaging the integrity of the bacteria, which may be one of the primary antibacterial mechanisms of **1**. Thus, we propose that the electrostatic interaction promoted **1** to capture the negatively charged bacteria cell wall, which led to severe destruction of the bacterial cells, induced intracellular components' leakage, and interfered with the bacteria's normal physiological activity, thereby leading to bacterial cell death.
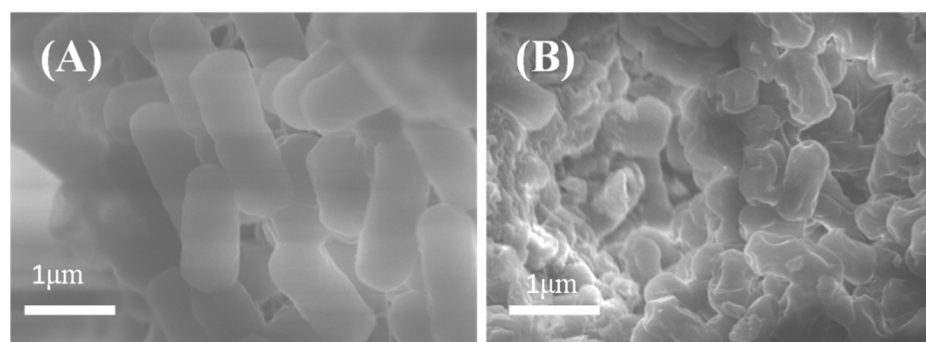
Figure 8. (**A**,**B**) SEM images of *E. coli* without treatment and with treatment with **1**.

It is generally assumed that antibacterial materials generally react with the bacterial cell wall/membrane, resulting in the leakage of intracellular substances such as K^+, DNA, and RNA, thus inducing damage to the cell membrane structures and disruption of the cell membrane integrity [48,49]. Significant changes were clearly observed in the experimental group (Figure 9A). Compared to the data changes (0.0913 ± 0.005) in the control group, the optical density of the 260 nm mensuration with the compound test group (0.2074 ± 0.0004) was obviously higher than the control group, indicating that **1** could damage the bacterial cell membrane. Meanwhile, the disruption of the bacterial cell and the leakage of cytoplasm induced by **1** were further proven by quantitative detection of the leakage of intracellular proteins, which is regarded as another momentous indicator of cytoplasmic leakage. The protein content in the test group in the presence of **1** was obviously higher than the control group (Figure S3B). High leakage of ribonucleic acid (RNA) and protein showed that **1** has significant antibacterial activity, enhancing the penetrability of the bacterial cell membrane and resulting in more leakage of intracellular RNA and proteins. Furthermore, the activity of the bacterial respiratory chains was tested to evaluate the probable antibacterial mechanism. The respiration chain dehydrogenase activity was significantly reduced in the test group after the treatment with **1** (Figure 9D), which indicates that the normal metabolism of bacteria was inhibited. Therefore, it can be inferred that **1** can break through the extracellular membrane and the barrier of the cytoplasm, destroying the respiratory chain dehydrogenase of bacterial cells and inhibiting the respiration of bacterial cells.

Apart from damaging the integrity of the bacterial structure via the direct physical contact between **1** and bacterial cells, oxidative stress is another significant antibacterial mechanism. Nitro blue tetrazolium (NBT) can be reduced to blue-violet formaldehyde in the presence of O^{2-}. Therefore, the index of the reactive oxygen species (ROS) content was determined by the production of blue-violet formaldehyde [50–52]. According to the previous literature, a high ROS content can lead to oxidative stress in bacteria cells [6,43], resulting in disruption of the bacterial cell membrane, intracellular substances, and so on. **1** induced an obviously higher level of ROS production than the control group (Figure 9B). Glutathione (GSH) can prevent cell damage caused by oxidative stress and is involved in protecting cells. However, antibacterial materials can convert sulfhydryl groups (-SH) of GSH to disulfide bonds (-S-S) to induce the oxidized process, and the content of -SH groups in GSH can be recognized by the Ellman method [53]. The data on the GSH content in the negative control group was almost unchanged (Figure 9C), meaning that the experimental conditions would not result in GSH oxidation. Meanwhile, the loss of GSH in the positive control group (H_2O_2) was about 67.1%, which is consistent with a previous literature report [46]. In contrast, the extent of GSH oxidation was reduced after the addition of **1**, and the oxidation ratio reached 34.6% after 15 min. The results showed that **1** may be released into the interior of the bacterial cell by the injured cell membrane or penetrate bacteria cells. Consequently, the oxidative stress response may be responsible for the bacterial cell apoptosis.
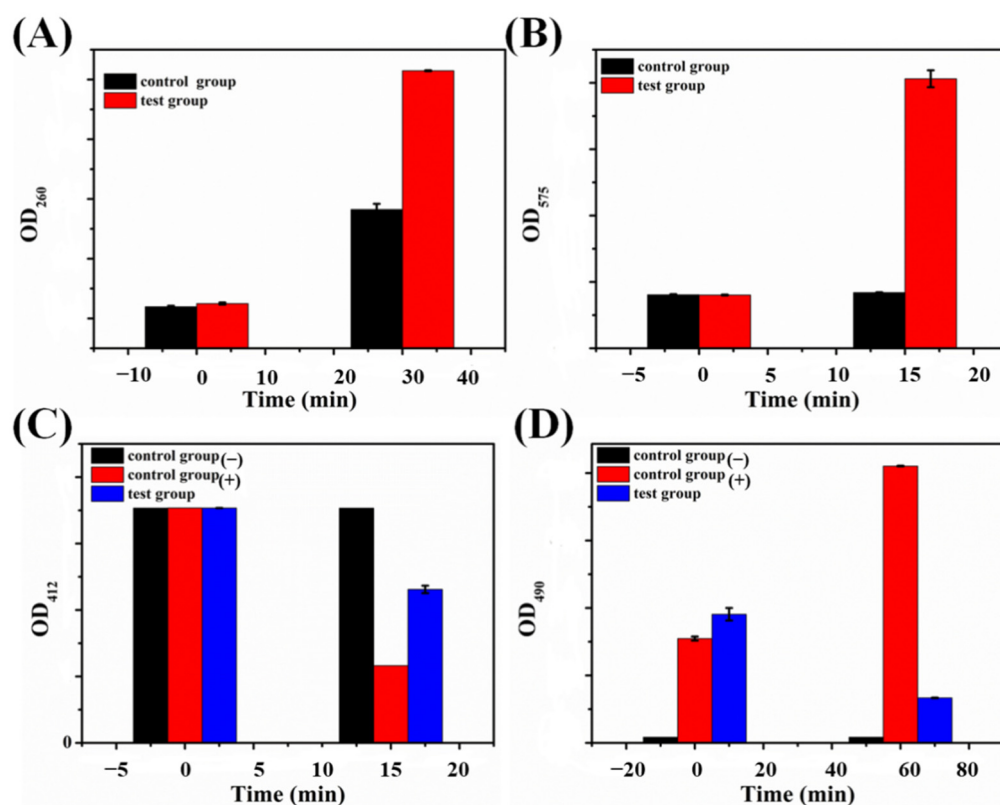
Figure 9. (**A**) Intracellular constituents of RNA leakage of *E. coli* at 260 nm. (**B**) Protein leakage of *E. coli* at 595 nm. (**C**) GSH oxidation at 412 nm induced by **1**. (**D**) The respiratory chain dehydrogenase activity of *E. coli* at 490 nm; parallel experiments were performed (mean ± SD, *n* = 3).

Specifically, there are several factors involved in bacterial cell death, including cell wall/membrane rupture, leakage of intracellular components, and the oxidative stress response. Based on our studies and previous literature [47,54], POMs can interact with the bacterial cell wall/membrane and destroy the integrity of the cell membrane, allowing intracellular substances to leak and disturb the normal cellular metabolism. In detail, the possible antibacterial action mechanisms of POMs are provided, as follows: (1) POMs interact with the bacterial cell wall, further localizing within or at the inner membrane of bacteria; (2) POMs are able to interfere with proteins that are responsible for some bacteria [23]; (3) as most POMs are highly redox active, they could impair the bacterial respiratory system by oxidizing some important electron carriers and thus affect ATP production [55]; and (4) POMs can also produce and elevate ROS by oxidizing proteins, lipids, GSH, and other bacterial compounds, which leads to the depletion of the GSH pool [56]. Based on the above analysis, it is concluded that bacterial death is mainly due to two points between membrane disruption and the oxidative stress process. On the one hand, $[Ni(L)(HL)]^+$ can interact with negatively charged bacterial cell membranes. On the other hand, the oxidizing $[PMo_{12}O_{40}]^{3-}$ anions may harm the bacterial respiratory system by oxidizing some important electron carriers [], thereby affecting ATP production. These two reasons cause the bacterial cell membrane to break down. Moreover, $[PMo_{12}O_{40}]^{3-}$ anions can produce ROS by oxidizing GSH, leading to the depletion of the GSH pool. The synergistic interactions of $[Ni(L)(HL)]^+$ and $[PMo_{12}O_{40}]^{3-}$ in **1** resulted in membrane disruption and the oxidative stress process. The proposed action mechanism of **1** against *E. coli* is presented in Scheme 1.
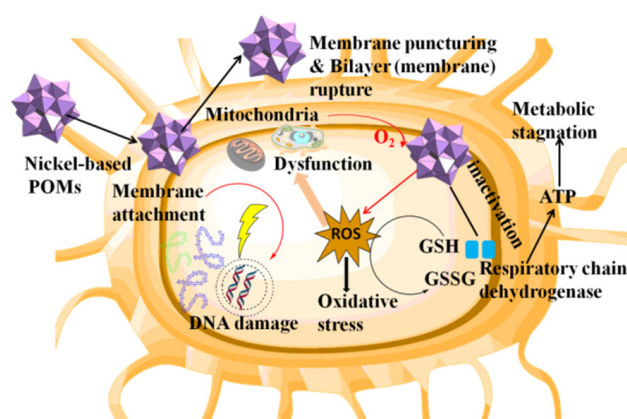
Scheme 1. The proposed mechanism of action of **1** against *E. coli*.

3. Materials and Methods

3.1. Materials

Sodium molybdate dihydrate ($Na_2MoO_4 \cdot 2H_2O$, 99%), nickel perchlorate hexahydrate ($Ni(ClO_4)_2 \cdot 6H_2O$, 99%), methyl alcohol (CH_3OH), acetonitrile (CH_3CN), and ethylene-diaminetetrakis (methylenephosphonic acid) (EDTMP, 98%) were available from Beijing Innochem Science & Technology Co., Ltd. (Beijing, China). Aqueous solutions of BF, MB, MO, and GV were obtained from J&K Scientific Ltd. (Beijing, China) and prepared using deionized water. Gram-negative bacteria (*E. coli*, *A. tumefaciens*) and Gram-positive bacteria (*S. aureus*, *B. subtilis*) were purchased from the China General Microbiological Culture Collection Center (Beijing, China).

3.2. Preparation of **1**

The ligand HL was synthesized according to the literature [26]. **1** was synthesized as follows: $Ni(ClO_4)_2 \cdot 6H_2O$ (0.475 g, 1.3 mmol), $Na_2MoO_4 \cdot 2H_2O$ (0.48 g, 2.0 mmol), EDTMP(0.35 g, 0.8 mmol), and HL (0.097 g, 0.5 mmol) were added to 60 mL of solvent with acetonitrile and water (1:2) and stirred continuously for 40 min at room temperature, which was followed by the use of NaOH (1 M) and HCl (1 M) solution to adjust pH to 3. Thereafter, the above mixture solution was tardily transferred to a 30-mL Teflon-lined autoclave, where such compound was heated at 110 °C for 72 h and subsequently cooled to room temperature. After filtration and washing with distilled water three times, the black quadrilateral crystals of **1** were obtained, and finally dried at 60 °C for 12 h (yield: 0.252 g, 72.2%, based on HL). EA and ICP (%): calcd for C 11.91, H 1.57, N 9.92, Ni 4.16, Mo 40.76 (%). Found for C 11.82, H 1.52, N 9.94, Ni 4.09, Mo 40.66 (%).

X-ray crystallography, antibacterial activity test, time-dynamic bactericidal test, adsorption performance of **1**, and antibacterial action investigation and characterization are provided in the Supplementary Materials. The crystal parameters, structure refinement data, and CCDC reference number (2119325) for **1** are listed in Table S1.

4. Conclusions

In conclusion, an Ni-based Keggin POM derived from $[PMo_{12}O_{40}]^{3-}$ and thiosemicarbazone was successfully synthesized using a facile hydrothermal method and systematically characterized. **1** revealed significant antibacterial activity against *E. coli*, with MIC values of 0.015 µg/mL and minor MIC values of 0.0019 µg/mL against *S. aureus*. Moreover, time-kill studies demonstrated the total bactericidal effect of **1** on the particular bacterium, revealing that the killing rate against S. aureus bacterium reached 97% after 4 h and almost 100% after 6 h. Further potential antimicrobial mechanisms were also investigated using the quantitative assay method. The synergistic interactions of $[Ni(L)(HL)]^+$ and $[PMo_{12}O_{40}]^{3-}$ in **1** resulted in membrane disruption and the oxidative stress response in the antimicrobial process. In addition, **1** showed significant activity in the removal of BF dyes (79.9%) within

90 min in wastewater. The pseudo-second-order kinetic model and the Freundlich isotherm model can properly describe the adsorption process. The BF adsorption is mainly governed by chemisorption and multilayer adsorption. This work displays more possibilities of POMs as multifunctional materials with antibacterial performance and dye adsorption properties for their application in water pollution treatment.

Supplementary Materials: The following supporting information can be downloaded at: https: //www.mdpi.com/article/10.3390/ijms23179651/s1. References [28,29,46,48–54] are cited in the supplementary materials.

Author Contributions: J.C.: Investigation, Data curation, Writing—original draft. M.L.: Investigation, Writing—review and editing. J.D.: Methodology. M.M.: Methodology. C.X.: Software. L.S.: Data curation, Validation, Writing—review and editing. P.M.: Writing—review and editing. All authors have read and agreed to the published version of the manuscript.

Institutional Review Board Statement: Not applicable.

Informed Consent Statement: Not applicable.

Data Availability Statement: Not applicable.

Conflicts of Interest: The authors declare that the research was conducted in the absence of any commercial or financial relationships that could be construed as a potential conflict of interest.

References

1. Qi, K.; Cheng, B.; Yu, J.; Ho, W. Review on the improvement of the photocatalytic and antibacterial activities of ZnO. *J. Alloy. Compd.* **2017**, *727*, 792–820. [CrossRef]
2. Fang, J.; Chen, Y.; Fang, C.; Zhu, L. Regenerable adsorptive membranes prepared by mussel-inspired co-deposition for aqueous dye removal. *Sep. Purif. Technol.* **2022**, *281*, 119876. [CrossRef]
3. Badvi, K.; Javanbakht, V. Enhanced photocatalytic degradation of dye contaminants with TiO_2 immobilized on ZSM-5 zeolite modified with nickel nanoparticles. *J. Clean. Prod.* **2021**, *280*, 124518. [CrossRef]
4. Cao, M.; Wang, S.; Hu, J.; Lu, B.; Wang, Q.; Zang, S. Silver Cluster-Porphyrin-Assembled Materials as Advanced Bioprotective Materials for Combating Superbacteria. *Adv. Sci.* **2022**, *9*, 2103721. [CrossRef]
5. Asad, M.; Wang, S.; Wang, Q.-Y.; Li, L.-K.; Anwar, M.I.; Younas, A.; Zang, S.-Q. Aqueous media ultra-sensitive detection of antibiotics via highly stable luminescent 3D Cadmium-based MOF. *New J. Chem.* **2021**, *45*, 20887–20894. [CrossRef]
6. Xing, C.; Chang, J.; Ma, M.; Ma, P.; Sun, L.; Li, M. Ultrahigh-efficiency antibacterial and adsorption performance induced by copper-substituted polyoxomolybdate-decorated graphene oxide nanocomposites. *J. Colloid Interface Sci.* **2022**, *612*, 664–678. [CrossRef]
7. Leng, B.; Zhang, X.L.; Chen, S.S.; Li, J.; Sun, Z.Q.; Ma, Z.Y.; Yang, W.J.; Zhang, B.C.; Yang, K.; Guo, S. Highly efficient visible-light photocatalytic degradation and antibacterial activity by GaN:ZnO solid solution nanoparticles. *J. Mater. Sci. Technol.* **2021**, *94*, 67–76. [CrossRef]
8. Ye, W.T.; Jiang, Y.; Liu, Q.; Xu, D.D.; Zhang, E.; Cheng, X.W.; Wan, Z.; Liu, C. The preparation of visible light-driven ZnO/Ag2MoO4/Ag nanocomposites with effective photocatalytic and antibacterial activity. *J. Alloy. Compd.* **2021**, *891*, 161898. [CrossRef]
9. Lv, C.; Chen, S.; Xie, Y.; Wei, Z.; Chen, L.; Bao, J.; He, C.; Zhao, W.; Sun, S.; Zhao, C. Positively-charged polyethersulfone nanofibrous membranes for bacteria and anionic dyes removal. *J. Colloid Interface Sci.* **2019**, *556*, 492–502. [CrossRef]
10. Xu, Y.T.; Lin, W.T.; Wang, H.; Guo, J.B.; Yuan, D.D.; Bao, J.X.; Sun, S.D.; Zhao, W.F.; Zhao, C.S. Dual-functional polyethersulfone composite nanofibrous membranes with synergistic adsorption and photocatalytic degradation for organic dyes. *Compos. Sci. Technol.* **2020**, *199*, 108353. [CrossRef]
11. Yadav, A.; Sharma, A.; Sharma, R.K. Mesoporous iron gallate nanocomplex for adsorption and degradation of organic dyes. *Colloids Surf. A Physicochem. Eng. Asp.* **2019**, *579*, 123694. [CrossRef]
12. Kong, Q.; Li, Z.G.; Ding, F.; Ren, X.H. Hydrophobic N-halamine based POSS block copolymer porous films with anti-bacterial and resistance of bacterial adsorption performances. *Chem. Eng. J.* **2021**, *410*, 128407. [CrossRef]
13. Malwal, D.; Gopinath, P. Efficient adsorption and antibacterial properties of electrospun CuO-ZnO composite nanofibers for water remediation. *J. Hazard. Mater.* **2017**, *321*, 611–621. [CrossRef] [PubMed]

14. Liu, Y.L.; Jia, J.; Gao, T.T.; Wang, X.L.; Yu, J.Y.; Wu, D.Q.; Li, F.X. One-pot fabrication of antibacterial beta-cyclodextrin-based nanoparticles and their superfast, broad-spectrum adsorption towards pollutants. *J. Colloid Interface Sci.* **2020**, *576*, 302–312. [CrossRef]

15. Li, J.F.; Chen, Z.J.; Zhou, M.C.; Jing, J.B.; Li, W.; Wang, Y.; Wu, L.X.; Wang, L.Y.; Wang, Y.Q.; Lee, M. Polyoxometalate-driven self-assembly of short peptides into multivalent nanofibers with enhanced antibacterial activity. *Angew. Chem. Int. Ed.* **2016**, *55*, 2592–2595. [CrossRef]

16. Liu, J.-X.; Zhang, X.-B.; Li, Y.-L.; Huang, S.-L.; Yang, G.-Y. Polyoxometalate functionalized architectures. *Coord. Chem. Rev.* **2020**, *414*, 213260. [CrossRef]

17. Gumerova, N.I.; Al-Sayed, E.; Krivosudský, L.; Čipčić-Paljetak, H.; Verbanac, D.; Rompel, A. Antibacterial Activity of Polyoxometalates Against Moraxella catarrhalis. *Front. Chem.* **2018**, *6*, 336. [CrossRef]

18. Zhao, M.; Fang, Y.; Ma, L.; Zhu, X.; Jiang, L.; Li, M.; Han, Q. Synthesis, characterization and in vitro antibacterial mechanism study of two Keggin-type polyoxometalates. *J. Inorg. Biochem.* **2020**, *210*, 111131. [CrossRef]

19. Tanuhadi, E.; Gumerova, N.I.; Prado-Roller, A.; Galanski, M.; Cipcic-Paljetak, H.; Verbanac, D.; Rompel, A. Aluminum-substituted Keggin germanotungstate $[HAl(H_2O)GeW_{11}O_{39}]^{4-}$ synthesis, characterization, and antibacterial activity. *Inorg. Chem.* **2021**, *60*, 28–31. [CrossRef]

20. Yao, L.; Zhang, L.; Wang, R.; Chou, S.; Dong, Z. A new integrated approach for dye removal from wastewater by polyoxometalates functionalized membranes. *J. Hazard. Mater.* **2016**, *301*, 462–470. [CrossRef]

21. Lesbani, A.; Taher, T.; Palapa, N.R.; Mohadi, R.; Rachmat, A. Mardiyanto Preparation and utilization of Keggin-type polyoxometalate intercalated Ni–Fe layered double hydroxides for enhanced adsorptive removal of cationic dye. *SN Appl. Sci.* **2020**, *2*, 1–4. [CrossRef]

22. Misra, A.; Castillo, I.F.; Müller, D.P.; González, C.; Eyssautier-Chuine, S.; Ziegler, A.; De La Fuente, J.M.; Mitchell, S.G.; Streb, C. Back Cover: Polyoxometalate-Ionic Liquids (POM-ILs) as Anticorrosion and Antibacterial Coatings for Natural Stones (Angew. Chem. Int. Ed. 45/2018). *Angew. Chem. Int. Ed.* **2018**, *57*, 14948. [CrossRef]

23. Bijelic, A.; Aureliano, M.; Rompel, A. The antibacterial activity of polyoxometalates: Structures, antibiotic effects and future perspectives. *Chem. Commun.* **2018**, *54*, 1153–1169. [CrossRef] [PubMed]

24. Xing, C.L.; Ma, P.T.; Zhao, M.; Chang, J.N.; Guo, X.Y.; Sun, L.; Li, M.X. Facile and green synthesis of decatungstate-based nickel(ii) complex coated onto modified Fe3O4 nanoparticles with enhanced antimicrobial activity against antibiotic-resistant bacteria. *CrystEngComm* **2021**, *23*, 3919–3928. [CrossRef]

25. King, A.P.; Gellineau, H.A.; Ahn, J.E.; MacMillan, S.N.; Wilson, J.J. Bis(thiosemicarbazone) complexes of cobalt(III): Synthesis, characterization, and anticancer potential. *Inorg. Chem.* **2017**, *56*, 6609–6623. [CrossRef]

26. Li, M.-X.; Chen, C.-L.; Ling, C.-S.; Zhou, J.; Ji, B.-S.; Wu, Y.-J.; Niu, J.-Y. Cytotoxicity and structure–activity relationships of four α-N-heterocyclic thiosemicarbazone derivatives crystal structure of 2-acetylpyrazine thiosemicarbazone. *Bioorganic Med. Chem. Lett.* **2009**, *19*, 2704–2706. [CrossRef]

27. Li, J.; Wang, B.; Chang, B.; Liu, J.; Zhu, X.; Ma, P.; Sun, L.; Li, M. One new hexatungstate-based binuclear nickel(II) complex with high selectivity adsorption for organic dyes. *J. Mol. Struct.* **2021**, *1231*, 129674. [CrossRef]

28. Dolomanov, O.V.; Bourhis, L.J.; Gildea, R.J.; Howard, J.A.K.; Puschmann, H. OLEX2: A complete structure solution, refinement and analysis program. *J. Appl. Cryst.* **2009**, *42*, 339–341. [CrossRef]

29. Sheldrick, G.M. SHELXT–integrated space-group and crystalstructure determination. *Acta Cryst.* **2015**, *A71*, 3–8.

30. Casanova, D.; Llunell, M.; Alemany, P.; Alvarez, S. The Rich Stereochemistry of Eight-Vertex Polyhedra: A Continuous Shape Measures Study. *Chem. A Eur. J.* **2005**, *11*, 1479–1494. [CrossRef]

31. Tian, A.; Ning, Y.; Ying, J.; Zhang, J.; Hou, X.; Li, T.; Wang, X. Highly efficient usage of the hydrothermal technique through the one-pot method to construct four Keggin-based compounds containing pendent ligands. *Dalton Trans.* **2015**, *44*, 10499–10507. [CrossRef] [PubMed]

32. Alizadeh, M.H.; Holman, K.T.; Mirzaei, M.; Razavi, H. Triprolinium 12-phosphomolybdate: Synthesis, crystal structure and properties of $[C_5H_{10}NO_2]_3[PMo_{12}O_{40}] \cdot 4.5H_2O$. *Polyhedron* **2019**, *2*, 5898–5904. [CrossRef]

33. Wang, J.; Chen, Y.; Cheng, N.; Feng, L.; Gu, B.-H.; Liu, Y. Multivalent Supramolecular Self-Assembly between β-Cyclodextrin Derivatives and Polyoxometalate for Photodegradation of Dyes and Antibiotics. *ACS Appl. Bio Mater.* **2019**, *2*, 5898–5904. [CrossRef] [PubMed]

34. Soares, J.C.S.; Gonçalves, A.H.A.; Zotin, F.M.; de Araújo, L.R.R.; Gaspar, A.B. Cyclohexene to adipic acid synthesis using heterogeneous polyoxometalate catalysts. *Mol. Catal.* **2018**, *458*, 223–229. [CrossRef]

35. Yasmina, I.; Sihem, M.; Dahbia, A.; Tassadit, M.; Catherine, M.-R.; Cherifa, R. Cyclohexanone oxidation over H3PMo12O40 heteropolyacid via two activation modes microwave irradiation and conventional method. *Bull. Chem. React. Eng.* **2019**, *14*, 427–435.

36. Tai, Y.-X.; Ji, Y.-M.; Lu, Y.-L.; Li, M.-X.; Wu, Y.-Y.; Han, Q.-X. Cadmium(II) and indium(III) complexes derived from 2-benzoylpyridine *N*(4)-cyclohexylthiosemicarbazone: Synthesis, crystal structures, spectroscopic characterization and cytotoxicity. *Synth. Met.* **2016**, *219*, 109–114. [CrossRef]

37. Tan, F.; Chen, H.; Yuan, R.; Zhang, X.; Chen, D. Co-Ni Basic Carbonate Nanowire/Carbon Nanotube Network With High Electrochemical Capacitive Performance via Electrochemical Conversion. *Front. Chem.* **2021**, *9*, 655025. [CrossRef]

38. Yu, J.G.; Hai, Y.; Cheng, B. Enhanced photocatalytic H_2-production activity of TiO_2 by $Ni(OH)_2$ cluster modification. *J. Phys. Chem. C* **2011**, *115*, 4953–4958. [CrossRef]

39. Haddad, M.E. Removal of Basic Fuchsin dye from water using mussel shell biomass waste as an adsorbent: Equilibrium, kinetics, and thermodynamics. *J. Taibah. Univ. Sci.* **2016**, *10*, 664–674. [CrossRef]

40. Xiong, W.P.; Zeng, Z.; Zeng, G.; Yang, Z.; Xiao, R.; Li, X.; Cao, J.; Zhou, C.; Chen, H.; Jia, M.; et al. Metal-organic frameworks derived magnetic carbon-αFe/Fe_3C composites as a highly effective adsorbent for tetracycline removal from aqueous solution. *Chem. Eng. J.* **2019**, *374*, 91–99. [CrossRef]

41. Tao, E.; Ma, D.; Yang, S.Y.; Hao, X. Graphene oxide-montmorillonite/sodium alginate aerogel beads for selective adsorption of methylene blue in wastewater. *J. Alloy. Compd.* **2020**, *832*, 154833.

42. He, R.; Xue, K.; Wang, J.; Yan, Y.; Peng, Y.; Yang, T.; Hu, Y.; Wang, W. Nitrogen-deficient g-C_3N_x/POMs porous nanosheets with P–N heterojunctions capable of the efficient photocatalytic degradation of ciprofloxacin. *Chemosphere* **2020**, *259*, 127465. [CrossRef]

43. Li, J.; Si, C.; Zhao, H.; Meng, Q.; Chang, B.; Li, M.; Liu, H. Dyes Adsorption Behavior of Fe_3O_4 Nanoparticles Functionalized Polyoxometalate Hybrid. *Molecules* **2019**, *24*, 3128. [CrossRef] [PubMed]

44. Cheng, X.; Sun, P.; Zhang, S.; Sun, D.; Jiang, B.; Wang, W.; Xin, X. Self-assembly of m-phenylenediamine and polyoxometalate into hollow-sphere and core-in-hollow-shell nanostructures for selective adsorption of dyes. *J. Mol. Liq.* **2019**, *287*, 110982. [CrossRef]

45. Wei, R.; Song, W.Y.; Yang, F.; Zhou, J.K.; Zhang, M.; Zhang, X.; Zhao, W.F.; Zhao, C.S. Bidirectionally pH-responsive zwitterionic polymer hydrogels with switchable selective adsorption capacities for anionic and cationic dyes. *Ind. Eng. Chem. Res.* **2018**, *57*, 8209–8219. [CrossRef]

46. Fang, Y.; Xing, C.; Zhan, S.; Zhao, M.; Li, M.; Liu, H. A polyoxometalate-modified magnetic nanocomposite: A promising antibacterial material for water treatment. *J. Mater. Chem. B* **2019**, *7*, 1933–1944. [CrossRef]

47. Li, X.; Sun, J.; Che, Y.; Lv, Y.; Liu, F. Antibacterial properties of chitosan chloride-graphene oxide composites modified quartz sand filter media in water treatment. *Int. J. Biol. Macromol.* **2019**, *121*, 760–773. [CrossRef]

48. Chen, C.Z.; Cooper, S.L. Interactions between dendrimer biocides and bacterial membranes. *Biomaterials.* **2002**, *23*, 3359–3368. [CrossRef]

49. He, M.Y.; Wu, T.; Pan, S.Y.; Xu, X.Y. Antimicrobial mechanism of flavonoids against Escherichia coli ATCC 25922 by model membrane study. *Appl. Surf. Sci.* **2014**, *305*, 515–521. [CrossRef]

50. Liu, S.B.; Zeng, T.Y.H.; Hofmann, M.; Burcombe, E.; Wei, J.; Jiang, R.R.; Kong, J.; Chen, Y. Antibacterial activity of graphite, graphite oxide, graphene oxide, and reduced graphene oxide: Membrane and oxidative stress. *ACS Nano* **2011**, *5*, 6971–6980. [CrossRef]

51. Zhang, M.Z.; Zhang, C.; Zhai, X.Y.; Luo, F.; Du, Y.P.; Yan, C.H. Antibacterial mechanism and activity of cerium oxide nanoparticles. *Sci China Mater.* **2019**, *62*, 1727–1739. [CrossRef]

52. Banerjee, M.; Mallick, S.; Paul, A.; Chattopadhyay, A.; Ghosh, S.S. Heightened reactive oxygen species generation in the antimicrobial activity of a three component iodinated chitosan-silver nanoparticle composite. *Langmuir* **2010**, *26*, 5901–5908. [CrossRef] [PubMed]

53. Riener, C.K.; Kada, G.; Gruber, H.J. Quick measurement of protein sulfhydryls with Ellman's reagent and with 4,4′-dithiodipyridine. *Anal Bioanal. Chem.* **2002**, *373*, 266–276. [CrossRef] [PubMed]

54. Mukherjee, S.; Chowdhury, D.; Kotcherlakota, R.; Patra, S.; Vinothkumar, B.; Bhadra, M.P.; Sreedhar, B.; Patra, C.R. Potential Theranostics Application of Bio-Synthesized Silver Nanoparticles (4-in-1 System). *Theranostics* **2014**, *4*, 316–335. [CrossRef]

55. Sami, P.; Anand, T.D.; Premanathan, M.; Rajasekaran, K. Vanadium(V)-substituted Keggin-type heteropolyoxotung-stophosphates as electron transfer and antimicrobial agents: Oxidation of glutathione and sensitization of MRSA to-wards β-lactam antibiotics. *Transit. Metal. Chem.* **2010**, *35*, 1019–1025. [CrossRef]

56. Soares, S.S.; Martins, H.; Duarte, R.O.; Moura, J.J.G.; Coucelo, J.; Gutiérrez-Merino, C.; Aureliano, M. Vanadium distribution, lipid peroxidation and oxidative stress markers upon decavanadate in vivo administration. *J. Inorg. Biochem.* **2007**, *101*, 80–88. [CrossRef]